symmetry

IMPACT FACTOR 2.2

CITESCORE 5.3

Review

Recent Progress in Antimatter Research with Heavy-Ion Collisions

Tan Lu, Junlin Wu and Hao Qiu

Topic Collection

Symmetry/Asymmetry in Baryon Decay: Polarization, Hyperon Asymmetry Parameters and CP Violation

Edited by
Prof. Dr. Xiongfei Wang

MDPI

https://doi.org/10.3390/sym18040693

symmetry

MDPI

Review

Recent Progress in Antimatter Research with Heavy-Ion Collisions

Tan Lu [1,2], Junlin Wu [2] and Hao Qiu [1,2,*]

[1] State Key Laboratory of Heavy Ion Science and Technology, Institute of Modern Physics, Chinese Academy of Sciences, Lanzhou 730000, China; lut@impcas.ac.cn
[2] School of Nuclear Science and Technology, University of Chinese Academy of Sciences, Beijing 101408, China; wujunlin@ucas.ac.cn
* Correspondence: qiuh@impcas.ac.cn

Abstract

Matter–antimatter asymmetry is a fundamental question in both astronomy and particle physics. Investigating antimatter is of great interest for testing the potential explanations of matter–antimatter asymmetry in our Universe. In relativistic heavy-ion collisions, the extremely high energy density and temperature are similar to the early Universe shortly after the Big Bang. In this paper, we review the recent progress in antimatter search and study heavy-ion collisions, with a focus on the RHIC-STAR and LHC-ALICE experiments, particularly the newly observed antimatter hypernuclei $^{4}_{\Lambda}\overline{\mathrm{H}}$ and $^{4}_{\Lambda}\overline{\mathrm{He}}$. The statistical thermal model and the coalescence production model can quantitatively describe the production yields and yield ratios, and the yield measurements of $^{4}_{\Lambda}\overline{\mathrm{H}}$, $^{4}_{\Lambda}\overline{\mathrm{He}}$ and their matter counterparts indicate the existence of spin-excited states of these (anti)hypernuclei. Furthermore, new measurements of the lifetimes of $^{3}_{\Lambda}\overline{\mathrm{H}}$, $^{4}_{\Lambda}\overline{\mathrm{H}}$ and their matter counterparts reveal no difference between a particle and its corresponding antiparticle, which validates the CPT theorem.

Keywords: antimatter; heavy-ion collision; hypernucleus; yield; lifetime

1. Introduction

The modern concept of antimatter originated from the negative energy solution of the Dirac equation for the electron [1]. Later, the anti-electron (positron) was discovered in 1932 by Anderson C. D. in a cosmic ray experiment [2]. Strong evidence shows that the current observable universe is dominated by matter [3]. However, the Big Bang theory predicts that equal amounts of matter and antimatter should have been produced in the early Universe. Astronomy observations, such as cosmic expansion [4] and cosmic microwave background [5,6], support a hot and dense early universe where matter and antimatter particle pairs are continuously created and annihilated. Thus, the net baryon number should be zero, implying matter–antimatter symmetry at the beginning of the Universe. As the Universe expands and cools, the annihilation process dominates. Since both creation and annihilation conserve the net baryon number, any observed matter–antimatter imbalance should originate from an asymmetry generated dynamically during cosmic evolution. Today, matter clearly dominates in the current observed Universe [3]. This well-known matter–antimatter asymmetry, also referred to as baryon asymmetry of the Universe (BAU), remains one of the fundamental open questions in both astronomy and particle physics. In 1967, physicist Sakharov A.D. proposed that matter–antimatter asymmetry could arise dynamically through the evolution of Universe rather than being imposed in initial conditions. He identified three necessary criteria, known as Sakharov's conditions, for a possible

Academic Editor: Ignatios Antoniadis

Received: 22 March 2026
Revised: 11 April 2026
Accepted: 13 April 2026
Published: 21 April 2026

baryon asymmetry mechanism: (i) baryon number violation, (ii) C and CP symmetry breaking, (iii) out of thermal equilibrium [7]. In principle, the Sakharov conditions can be satisfied within the framework of the Standard Model, but the resulting asymmetry is too small to account for the observed matter dominance [3]. This discrepancy underscores the need for physics beyond the Standard Model and motivates continued experimental and theoretical investigations into antimatter.

Symmetry plays an important role in physics. In a local quantum field with Lorentz invariance, physical laws under the combined operator of charge conjugation (C), parity inversion (P), and time reversal (T) are invariant, known as CPT symmetry. The CPT theorem guarantees that matter and antimatter particles possess some identical intrinsic properties, such as mass and lifetime. Any measurable difference in these properties between matter and antimatter would signal CPT violation. To date, no CPT violation has been observed despite numerous high-precision experimental tests [8–13]. In heavy-ion collisions, the first measurement of the strong interaction between antiprotons, obtained by using correlation functions, reveals the interaction is attractive. The scattering length and the effective range of the interaction are consistent with the corresponding proton–proton interaction within uncertainties [14]; the results validate the CPT symmetry.

In the current Universe, antiparticles are difficult to produce and detect due to rapid annihilation upon contact with matter. Two approaches are employed to study antiparticles: cosmic ray and accelerator-based collisions. High-energy cosmic rays interacting with the interstellar medium can produce antiparticles, such as antiprotons, which are detected by space-based experiments [15]. However, antimatter nuclei with a mass number $A \geq 2$ have so far only been observed in heavy-ion collision experiments. Heavy-ion collisions recreate the extremely high temperature and energy density similar to those of the early Universe shortly after the Big Bang, enabling the copious production of antimatter. As the fireball expands and cools, a fraction of the produced antiparticles can decouple from the medium before annihilation, and then be observed by the detectors [16].

In heavy-ion collisions, (anti)hypernuclei can be produced. Containing at least one hyperon, hypernuclei serve as a unique probe to the hyperon–nucleon (Y-N) interaction, which is crucial for understanding the equation of state of dense matter in neutron stars [17]. The lightest hypernucleus is ${}^{3}_{\Lambda}\mathrm{H}$, which was first observed in nuclear emulsion exposed to a cosmic ray [18]. Its corresponding antiparticle ${}^{3}_{\overline{\Lambda}}\overline{\mathrm{H}}$ was observed in heavy-ion collisions by the STAR Collaboration [19]. Precise measurements of the mass and binding energy of ${}^{3}_{\Lambda}\mathrm{H}$ and ${}^{3}_{\overline{\Lambda}}\overline{\mathrm{H}}$ show excellent agreement between particle and antiparticle [20], providing a validation of the CPT theorem.

In this paper, we review the recent experimental progress in antimatter research from the STAR experiment at the RHIC and the ALICE experiment at the LHC, with particular emphasis on the newly discovered antimatter hypernuclei ${}^{4}_{\overline{\Lambda}}\overline{\mathrm{H}}$ and ${}^{4}_{\overline{\Lambda}}\overline{\mathrm{He}}$. We discuss their measured properties, including lifetimes and production yields, as well as the underlying production mechanisms inferred from data.

2. Experiment

Historical milestones in antimatter discovery are summarized in Figure 1. The first antiparticle, the positron, was discovered in a cosmic ray experiment using a cloud chamber. Observed tracks had the same mass-to-charge ratio as the electron but curved in the opposite direction [2]. Later, as synchrotron technology was employed in experiments, heavier antiparticles were subsequently discovered: antiproton ($\overline{p}$) [21], antineutron ($\overline{n}$) [22], and antilambda ($\overline{\Lambda}$) [23]. Then composite antimatter nuclei with baryon numbers of 2 and 3, including antideuteron ($\overline{d}$) [24,25], antitriton ($\overline{t}$) [26] and antihelium-3 (${}^{3}\overline{\mathrm{He}}$) [27], were discovered. Decades later, the RHIC-STAR collaboration reported the first observation of

antimatter hypernucleus ${}^{3}_{\Lambda}\overline{\mathrm{H}}$ in 2010 [19], followed by the discovery of ${}^{4}\overline{\mathrm{He}}$ in 2011 [28]. A comprehensive overview of the antimatter in heavy-ion collisions can be found in [29]. In recent years, STAR [30] and ALICE [31] experiments have led the frontier of antimatter research with heavy-ion collisions. The STAR collaboration reports the heaviest antimatter hypernucleus observed so far, ${}^{4}_{\Lambda}\overline{\mathrm{H}}$ [16]. And the ALICE collaboration confirms the existence of ${}^{4}_{\Lambda}\overline{\mathrm{H}}$ and presents evidence for its isobaric partner, ${}^{4}_{\Lambda}\overline{\mathrm{He}}$ [32].

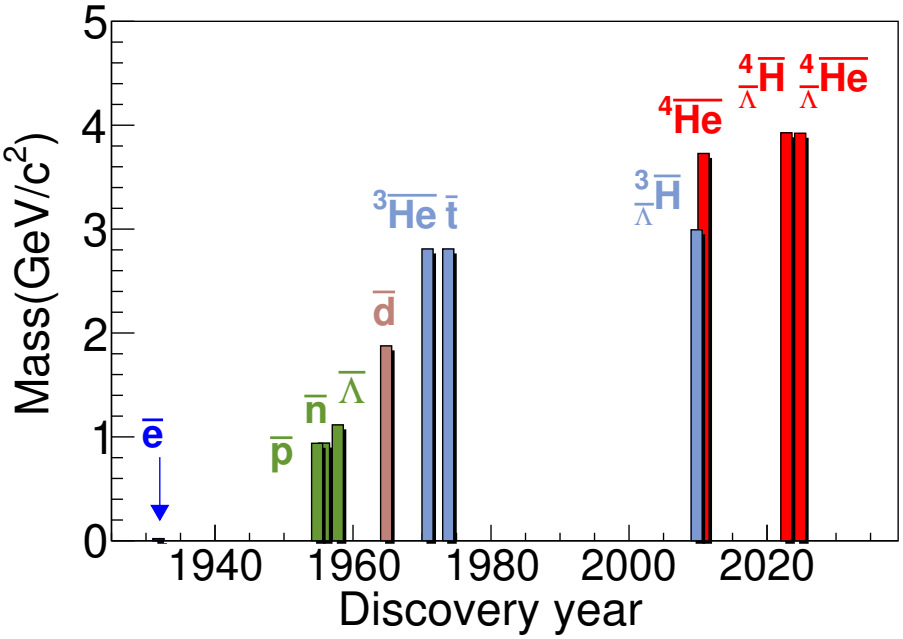

Figure 1. Antiparticles' mass vs. discovery year. Different color represents different baryon number.

2.1. STAR Detector at RHIC

STAR [30] is one of the four major detectors at the RHIC facility. A schematic of the detector system is shown in Figure 2. The main tracking system is the gas-filled cylindrical Time Projection Chamber (TPC). With a magnetic field of 0.5 T parallel to the beam direction, particle momentum information can be obtained. TPC can also acquire energy loss (dE/dx) information. Different charged particles exhibit different energy loss. Based on the Bethe–Bloch formula, as implemented in Bichsel theory [33], charged particle species can be identified by TPC. Since 2018, the inner region of the TPC has been upgraded (iTPC), extending the charged particle pseudorapidity η coverage from $|\eta| < 1.0$ to $|\eta| < 1.5$ with 2π azimuthal coverage.

The Time of Flight (TOF) detector provides additional particle identification ability. The whole TOF system consists of the barrel TOF and the vertex position detector (VPD). The barrel TOF, with $|\eta| < 0.96$ and 2π azimuthal coverage, uses the start time provided by the VPD detector. The TOF measurements significantly enhance STAR's separation ability for pions, kaons and protons. Along the beam line, a Forward Silicon Tracker (FST), small-strip Thin Gap Chamber (sTGC), Event Plane Detector (EPD) and Forward Calorimeter System (FCS) are installed. Around the beam, a Barrel Electromagnetic Calorimeter (BEMC) and Muon Telescope Detector (MTD) are installed. Details of sub-detector systems of STAR can be found in [30].

STAR is designed primarily to explore the properties of quark–gluon plasma (QGP), a deconfined state of matter that existed shortly after the Big Bang. Beam Energy Scan phases I and II (BES-I, BES-II), including the Fixed-Target program (FXT), have yielded fruitful results on the QCD phase diagram and hadron properties [34–39].

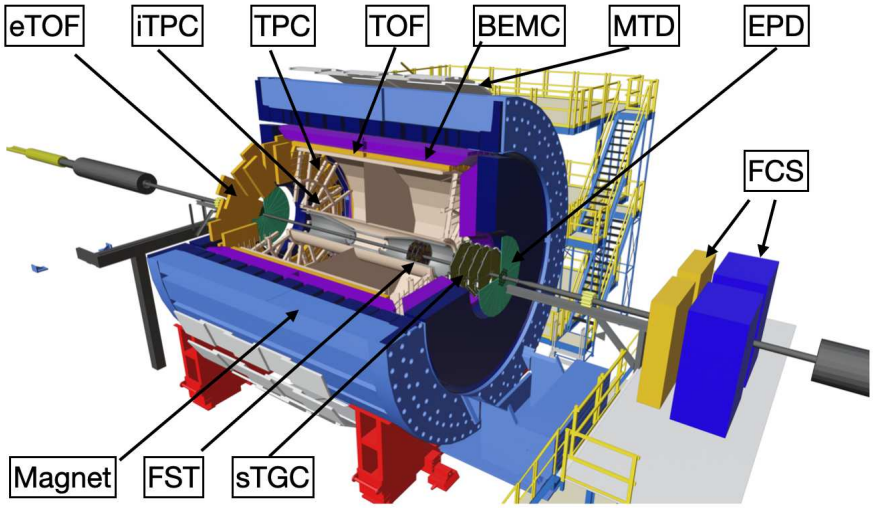

Figure 2. A schematic of the STAR detector.

2.2. ALICE Detector at LHC

ALICE [31] is a dedicated heavy-ion detector at the LHC at CERN, designed to study the properties of quark–gluon plasma under extreme high-temperature conditions. A schematic of the ALICE detector is shown in Figure 3. The ALICE experiment delivers excellent performance despite the thousands of particles produced in ultra-relativistic Pb+Pb collisions, as well as in smaller collision systems such as p+p collisions. The inner tracking system (ITS) [40] is at the center of the entire detector system, which provides precise reconstruction of the positions of primary and secondary vertices.

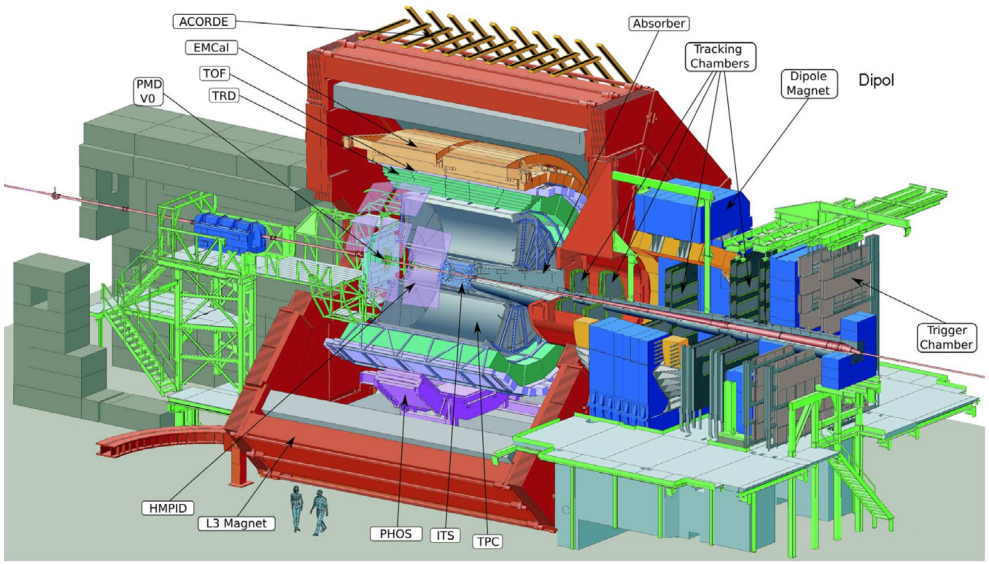

Figure 3. A schematic of the ALICE detector.

ALICE's main tracking system is the TPC [41], which reconstructs charged particle trajectories and measures their momenta in a 0.5 T solenoidal magnetic field aligned with the beam line. The TPC provides up to 159 three-dimensional space points per track, enabling high-precision tracking over full azimuthal coverage and a wide pseudorapidity range ($|\eta| < 0.9$). Additionally, the specific energy loss (dE/dx) measured along the track follows the Bethe–Bloch formula, allowing the discrimination of different charged particle species.

π, K and p identification is significantly enhanced by the TOF detector, which precisely measures the time for particles to reach the TOF detector from the collision vertex, combined with the momenta information from the TPC. The TOF detector achieves excellent separation power across a broad momentum range. From the beam line outward, the High-Momentum Particle IDentification (HMPID) PHOton Spectrometer (PHOS), Electro-Magnetic Calorimeter (EMCal) and ALICE COsmic Ray DEtector (ACORDE) are arranged. Details of other sub-detector systems can be found in [31].

Operating at TeV-scale center-of-mass energies in Pb+Pb collisions, ALICE offers a unique platform to probe the thermodynamic and transport properties of the QGP under extreme conditions. The ALICE collaboration has produced significant results in heavy flavor physics and hadron properties [42–47].

3. Results

3.1. Antimatter Hypernucleus Signals

In heavy-ion collisions, hypernucleus candidates can be reconstructed using the decayed charged daughter particles with their 3D momenta and masses. Specifically, the decay channels of ${}^{4}_{\Lambda}\overline{\mathrm{H}}$ and ${}^{4}_{\Lambda}\overline{\mathrm{He}}$ used in the analyses are ${}^{4}_{\Lambda}\overline{\mathrm{H}} \rightarrow {}^{4}\ \overline{\mathrm{He}} + \pi^{+}$ and ${}^{4}_{\Lambda}\overline{\mathrm{He}} \rightarrow {}^{3}\ \overline{\mathrm{He}} + \overline{\mathrm{p}} + \pi^{+}$, respectively.

The STAR collaboration reports the heaviest observed antimatter hypernuclues ${}^{4}_{\Lambda}\overline{\mathrm{H}}$ [16]. The invariant mass distribution of ${}^{4}_{\Lambda}\overline{\mathrm{H}}$ is shown in Figure 4. U+U, Au+Au, Ru+Ru and Zr+Zr collisions with energies of $\sqrt{s_{NN}} = 193$ GeV (U+U) and $\sqrt{s_{NN}} = 200$ GeV (other systems) are used in the measurement. After background subtraction, 15.6 ± 4.7 ${}^{4}_{\Lambda}\overline{\mathrm{H}}$ signal candidates were observed. The significance calculation is based on an asymptotic formula $Z = \sqrt{2[N_{Sig} + N_{Bg} ln(1 + \frac{N_{Sig}}{N_{Bg}}) - N_{Sig}]}$ [48]. Here Z_{count} is obtained with a direct counting of the signal N_{Sig} and background N_{Bg} within a certain invariant mass range, while for Z_{shape} a fitting function is applied to obtain the N_{Sig} and N_{Bg}. The derived significances are $Z_{count} = 4.8\sigma$ and $Z_{shape} = 4.7\sigma$.

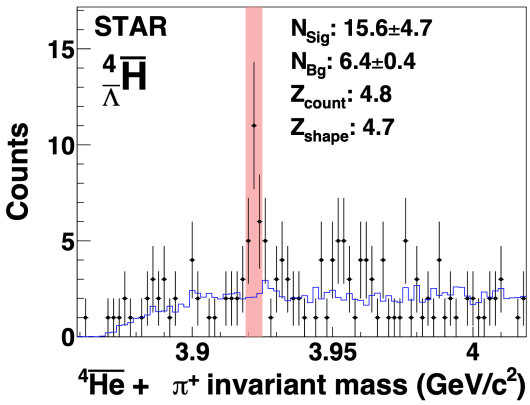

Figure 4. Plot is reproduced from [16]. Invariant mass distribution of ${}^{4}\overline{\mathrm{He}} + \pi^{+}$ with the ${}^{4}_{\Lambda}\overline{\mathrm{H}}$ signal in a combination of U+U, Au+Au, Ru+Ru and Zr+Zr collisions at $\sqrt{s_{NN}} = 193$ GeV (U+U) and $\sqrt{s_{NN}} = 200$ GeV (other systems) at STAR. The black points show signal candidates. The blue curve represents the background distribution constructed by randomly rotating one of the daughter tracks. The red band marks the signal-invariant mass region. Reproduced with permission from Springer Nature. License number: 6253050458017.

The ALICE collaboration also reports antimatter hypernuclei with a baryon number of 4 in Pb+Pb collisions at $\sqrt{s_{NN}} = 5.02$ TeV. The evidence for ${}^{4}_{\Lambda}\overline{\mathrm{He}}$ and the observation of ${}^{4}_{\Lambda}\overline{\mathrm{H}}$ are presented. The significances for ${}^{4}_{\Lambda}\overline{\mathrm{He}}$ and ${}^{4}_{\Lambda}\overline{\mathrm{H}}$ are 3.5σ and 4.5σ respectively, as shown in Figure 5. These findings from two independent experiments provide cross-validation for

the existence of ${}^{4}_{\Lambda}\overline{\mathrm{H}}$. The newly discovered antimatter particles ${}^{4}_{\Lambda}\overline{\mathrm{H}}$ and ${}^{4}_{\Lambda}\overline{\mathrm{He}}$ bring a new opportunity for studying antimatter properties, such as production yields and lifetimes, and for testing matter–antimatter symmetry in the hypernucleus sector.

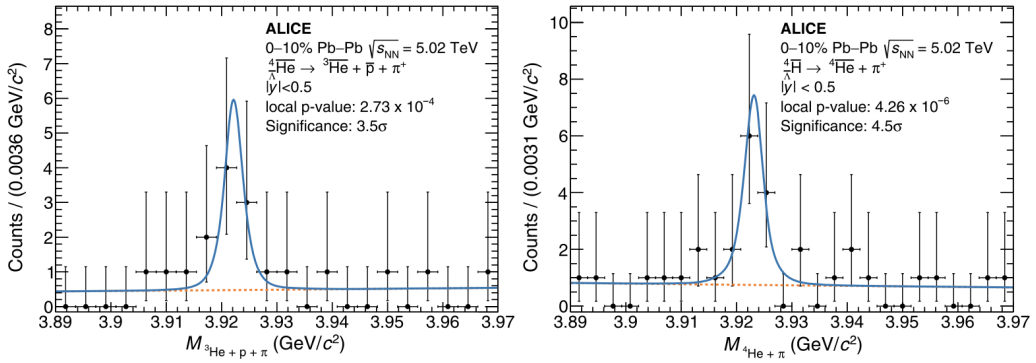

Figure 5. Plots are from [32]. Invariant mass distributions of ${}^{3}\overline{\mathrm{He}} + p + \pi^{+}$ with the ${}^{4}_{\Lambda}\overline{\mathrm{He}}$ signal (**left**) and of ${}^{4}\overline{\mathrm{He}} + \pi^{+}$ with the ${}^{4}_{\Lambda}\overline{\mathrm{H}}$ signal (**right**) in Pb+Pb collisions at $\sqrt{s_{NN}} = 5.02$ TeV at ALICE. Black points show signal candidates. Blue curves are the fitting lines, and the orange dashed lines show the fitting backgrounds.

3.2. Yield

Hypernucleus yields are related to the underlying particle production mechanisms. In heavy-ion collisions, hypernucleus production can be described by the coalescence model [28,49]. This model assumes that hypernuclei are produced near the kinetic freeze-out stage of the fireball evolution when p, n, and Λ are close in both coordinate and momentum space [50]. Alternatively, particle yields can also be well described by the statistical thermal model [51–53], which assumes that particles are produced from a system in chemical and thermal equilibrium. Global parameters such as temperature and baryon chemical potential can be extracted by simultaneously fitting all measured particle yields. The differences between the thermal model and the coalescence model have been systematically discussed and compared in [54].

Various particle yield ratios are presented in Figure 6 by the STAR experiment [16]. The yield ratios can largely eliminate the biases caused by different collision systems. Generally, all yield ratios between antiparticles and their corresponding particles are less than unity, reflecting the net-positive baryon number of the initial colliding nuclei. The statistic thermal model [51] can quantitatively describe the measured yield ratios. Notably, the yield ratios from experimental data exhibit the following scaling relationships: $\frac{{}^{3}\overline{\mathrm{He}}}{{}^{3}\mathrm{He}} \times \frac{\overline{\mathrm{p}}}{\mathrm{p}} \approx \frac{{}^{4}\overline{\mathrm{He}}}{{}^{4}\mathrm{He}}$, $\frac{{}^{3}_{\Lambda}\overline{\mathrm{H}}}{{}^{3}_{\Lambda}\mathrm{H}} \times \frac{\overline{\mathrm{p}}}{\mathrm{p}} \approx \frac{{}^{4}_{\Lambda}\overline{\mathrm{H}}}{{}^{4}_{\Lambda}\mathrm{H}}$, $\frac{{}^{4}_{\Lambda}\mathrm{H}}{{}^{4}\mathrm{He}} \approx 4 \times \frac{{}^{3}_{\Lambda}\mathrm{H}}{{}^{3}\mathrm{He}}$ and $\frac{{}^{4}_{\Lambda}\overline{\mathrm{H}}}{{}^{4}\overline{\mathrm{He}}} \approx 4 \times \frac{{}^{3}_{\Lambda}\overline{\mathrm{H}}}{{}^{3}\overline{\mathrm{He}}}$. These ratios are chosen so that the numbers of net constituent (anti-)nucleons and (anti-)Λ hyperons are consistent between the left- and right-hand sides of the equations. Thus, these scaling relationships are naturally expected within the coalescence framework when neglecting details such as the different sizes of the (anti)(hyper)nuclei. The factor 4 arises from the spin-degeneracy. ^{4}He and ${}^{4}\overline{\mathrm{He}}$ possess only a spin-0 ground state, while ${}^{4}_{\Lambda}$H and ${}^{4}_{\Lambda}\overline{\mathrm{H}}$ have spin-0 (ground) and spin-1 (excited) states. The excited state with a spin degeneracy factor of 3 can electromagnetically decay into the spin ground state, which increases the total measured yields by approximately a factor of 4. In general, the yield ratios can be well reproduced by the thermal model and are consistent with the expectations of the coalescence model.

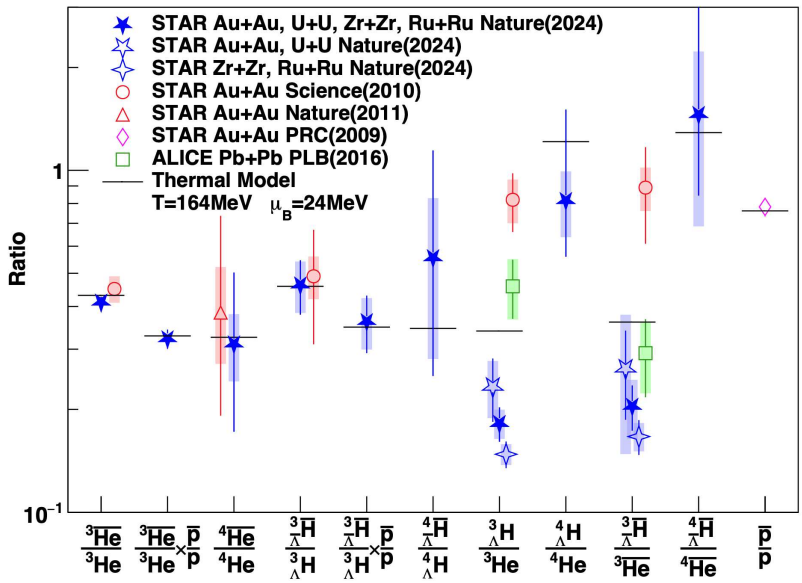

Figure 6. Plot is reproduced from [16]. The other references are [19,28,55,56]. Yield ratios for different particles from the STAR experiment. Reproduced with permission from Springer Nature. License number: 6253050458017.

In the ALICE experiment, the Statistical Hadron Model (SHM) [53] is employed to constrain the spin states of hypernuclei by comparing predicted and measured yields. The SHM model is a thermal model which explicitly accounts for spin degeneracy in its yield calculations. As shown in Figure 7, the ALICE collaboration measured yields and masses of the ${}^{4}_{\Lambda}\overline{\mathrm{H}}$ and ${}^{4}_{\Lambda}\overline{\mathrm{He}}$. The production yield dN/dy can be quantitatively reproduced by the SHM model only when spin-excited states are included. However, the coalescence calculation tends to underestimate the production yield of (anti)hypernuclei and (anti)nuclei measured by the ALICE collaboration [32,57]. If only the spin-0 ground state is assumed, the SHM model underpredicts the data by 2.2σ and 2.3σ for ${}^{4}_{\Lambda}\overline{\mathrm{He}}$ and ${}^{4}_{\Lambda}\overline{\mathrm{H}}$, respectively. Both STAR and ALICE data indicate ${}^{4}_{\Lambda}\overline{\mathrm{H}}$ has a spin-1 excited state.

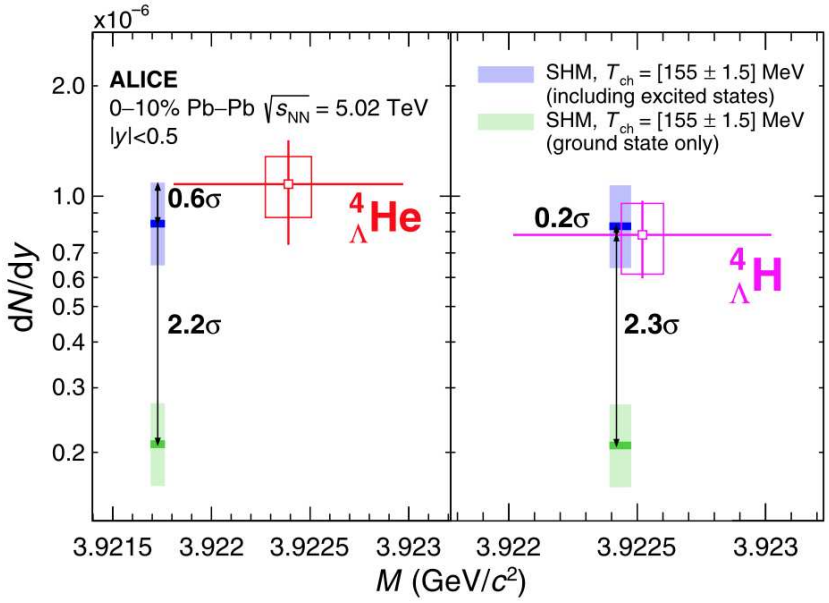

Figure 7. Plots are from [32]. (Anti)${}^{4}_{\Lambda}$He (**left**) and (anti)${}^{4}_{\Lambda}$H (**right**) integrated production yields vs. masses from the ALICE experiment. Results are averaged by particles and antiparticles for corresponding hypernucleus.

3.3. Lifetime Measurements

According to the CPT theorem, the lifetime of a particle and its corresponding antiparticle should be identical. Therefore, precision comparisons of the lifetimes of hypernuclei and their antimatter analogs provide a stringent test of CPT symmetry and may offer insights into the origin of the matter–antimatter asymmetry in the Universe. In heavy-ion collision experiments, hypernuclear lifetime is one of the key properties for investigating hyperon–nucleon interactions [58]. Due to the weak decay, the typical lifetime of a hypernucleus is on the order of $\sim 10^2$ ps, which is long enough to be experimentally accessible. The STAR Collaboration has measured the lifetimes of both matter and antimatter hypernuclei ${}^{3}_{\Lambda}\mathrm{H}$, ${}^{3}_{\bar{\Lambda}}\overline{\mathrm{H}}$, ${}^{4}_{\Lambda}\mathrm{H}$ and ${}^{4}_{\bar{\Lambda}}\overline{\mathrm{H}}$. As shown in the left panel of Figure 8, the lifetime τ is extracted by $N(t) = N_0 exp(-t/\tau) = N_0 exp(-(L/\beta\gamma)/\tau)$, where L is the hypernuclei decay length and $\beta\gamma$ is determined by the hypernucleus momentum. The extracted lifetime results for these (anti)hypernuclei are summarized in the right panel of Figure 8: $\tau({}^{3}_{\Lambda}\mathrm{H}) = 254 \pm 28(\mathrm{stat.}) \pm 14(\mathrm{sys.})$ ps, $\tau({}^{3}_{\bar{\Lambda}}\overline{\mathrm{H}}) = 238 \pm 33(\mathrm{stat.}) \pm 28(\mathrm{sys.})$ ps, $\tau({}^{4}_{\Lambda}\mathrm{H}) = 188 \pm 89(\mathrm{stat.}) \pm 37(\mathrm{sys.})$ ps, $\tau({}^{4}_{\bar{\Lambda}}\overline{\mathrm{H}}) = 170 \pm 72(\mathrm{stat.}) \pm 34(\mathrm{sys.})$ ps. This is the first measurement for the lifetime of ${}^{3}_{\bar{\Lambda}}\overline{\mathrm{H}}$ and ${}^{4}_{\bar{\Lambda}}\overline{\mathrm{H}}$. The measured lifetimes of ${}^{3}_{\Lambda}\mathrm{H}$ and ${}^{4}_{\Lambda}\mathrm{H}$ are consistent with world averaged data, and measured hypernuclei lifetimes are shorter than free Λ lifetime. The lifetime differences measured in the STAR between the hypernuclei and antimatter hypernuclei are $\tau({}^{3}_{\Lambda}\mathrm{H}) - \tau({}^{3}_{\bar{\Lambda}}\overline{\mathrm{H}}) = 16 \pm 43(\mathrm{stat.}) \pm 20(\mathrm{sys.})$ps and $\tau({}^{4}_{\Lambda}\mathrm{H}) - \tau({}^{4}_{\bar{\Lambda}}\overline{\mathrm{H}}) = 18 \pm 115(\mathrm{stat.}) \pm 46(\mathrm{sys.})$. Both results are consistent with zero within uncertainties, indicating no significant lifetime difference between the hypernuclei and their corresponding antihypernuclei.

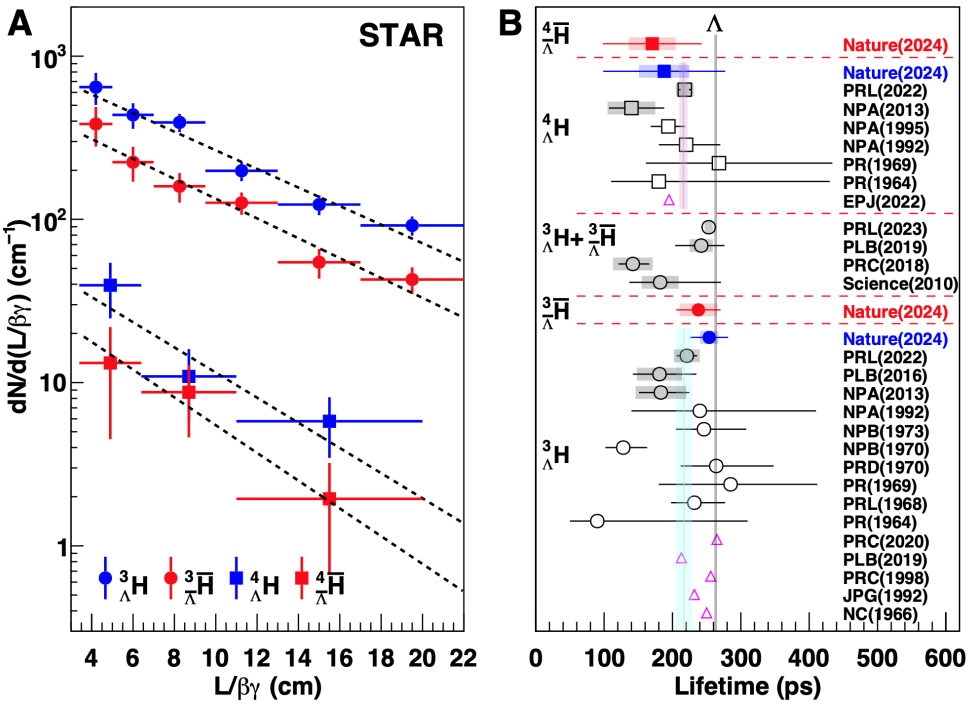

Figure 8. Plots are reproduced from [16]. The other references are [13,19,49,56,59–74]. (**A**) Λ yield in different $L/(\beta\gamma)$ with detector efficiency correction. (**B**) Measured lifetime of ${}^{3}_{\Lambda}\mathrm{H}$, ${}^{3}_{\bar{\Lambda}}\overline{\mathrm{H}}$, ${}^{4}_{\Lambda}\mathrm{H}$ and ${}^{4}_{\bar{\Lambda}}\overline{\mathrm{H}}$. Reproduced with permission from Springer Nature. License number: 6253050458017.

The ALICE collaboration has measured the relative lifetime difference between ${}^{3}_{\Lambda}\mathrm{H}$ and ${}^{3}_{\bar{\Lambda}}\overline{\mathrm{H}}$ [13]. The result is $\frac{\tau({}^{3}_{\Lambda}\mathrm{H}) - \tau({}^{3}_{\bar{\Lambda}}\overline{\mathrm{H}})}{\tau({}^{3}_{\Lambda}\mathrm{H})} = 0.03 \pm 0.07(\mathrm{stat.}) \pm 0.04(\mathrm{sys.})$. No lifetime difference is observed, which is consistent with the STAR measurement. These results constitute a new test of the CPT symmetry at the hypernucleus level.

4. Summary and Outlook

In summary, the STAR and ALICE collaborations are actively investigating antimatter with heavy-ion collisions, and the antimatter hypernucleus ${}^{4}_{\Lambda}\overline{\mathrm{H}}$ has been observed by both STAR and ALICE experiments. The ALICE collaboration has also presented evidence for ${}^{4}_{\Lambda}\overline{\mathrm{He}}$. Yield measurements strongly suggest the existence of spin-excited states in ${}^{4}_{\Lambda}\overline{\mathrm{H}}$ and ${}^{4}_{\Lambda}\overline{\mathrm{He}}$. Additionally, yield ratio measurements from the STAR collaboration support a coalescence-based production mechanism for light (anti)hypernuclei. Precision lifetime measurements of ${}^{3}_{\Lambda}\mathrm{H}$, ${}^{3}_{\Lambda}\overline{\mathrm{H}}$, ${}^{4}_{\Lambda}\mathrm{H}$ and ${}^{4}_{\Lambda}\overline{\mathrm{H}}$ show no statistically significant difference between matter and antimatter hypernuclei lifetimes, validating the CPT symmetry.

Recently, the STAR collaboration has finished collecting approximately 20.1 billion minimum-bias Au+Au collision events at $\sqrt{s_{NN}} = 200$ GeV over Run 23–25. Meanwhile, ALICE is in the final phase of Run 3 data taking, which employs continuous readout and a new silicon pixel tracker for the ITS2 detector. These upgrades have significantly enhanced ALICE's data-taking rate and tracking precision. These high-statistics datasets will enable more precise measurements of rare antimatter nuclei, open the door to the discovery of even heavier antimatter particles, and potentially deepen our understanding of fundamental symmetries and the origin of the matter–antimatter asymmetry in the Universe.

Author Contributions: Conceptualization, writing and review, T.L., J.W. and H.Q. All authors have read and agreed to the published version of the manuscript.

Funding: This review is supported by the Chinese Academy of Sciences Project for Young Scientists in Basic Research No. YSBR-088.

Data Availability Statement: The original data have been made publicly available by the referred collaborations.

Conflicts of Interest: The authors declare no conflicts of interest.

References

1. Dirac, P.A.M. The quantum theory of the electron. *Proc. Roy. Soc. A* **1928**, *117*, 610. [CrossRef]
2. Anderson, C.D. The Positive Electron. *Phys. Rev.* **1933**, *43*, 491–494. [CrossRef]
3. Canetti, L.; Drewes, M.; Shaposhnikov, M. Matter and antimatter in the universe. *New J. Phys.* **2012**, *14*, 095012. [CrossRef]
4. Hubble, E.A. relation between distance and radial velocity among extra-galactic nebulae. *Proc. Natl. Acad. Sci. USA* **1929**, *15*, 168–173. [CrossRef]
5. Penzias, A.A.; Wilson, R.W. A Measurement of Excess Antenna Temperature at 4080 Mc/s. *Astrophys. J.* **1965**, *142*, 419–421. Available online: https://api.semanticscholar.org/CorpusID:120759902 (accessed on 21 March 2026). [CrossRef]
6. Wilkinson, D.T. Measurement of the Cosmic Microwave Background at 8.56-mm Wavelength. *Phys. Rev. Lett.* **1967**, *19*, 1195–1198. [CrossRef]
7. Sakharov, A.D. Violation of CP invariance, C asymmetry, and baryon asymmetry of the universe. *Sov. Phys. Usp.* **1991**, *34*, 392. [CrossRef]
8. Abouzaid, E.; Arenton, M.; Barker, A.R.; Barrio, M.; Bellantoni, L.; Blucher, E.; Bock, G.J.; Bown, C.; Cheu, E.; Coleman, R.; et al. Precise measurements of direct CP violation, CPT symmetry, and other parameters in the neutral kaon system. *Phys. Rev. D* **2011**, *83*, 092001. [CrossRef]
9. Mittleman, R.K.; Ioannou, I.I.; Dehmelt, H.G.; Russell, N. Bound on CPT and Lorentz Symmetry with a Trapped Electron. *Phys. Rev. Lett.* **1999**, *83*, 2116. [CrossRef]
10. Bennett, G.W.; Bousquet, B.; Brown, H.N.; Bunce, G.; Carey, R.M.; Cushman, P.; Danby, G.T.; Debevec, P.T.; Deile, M.; Deng, H.; et al. Search for Lorentz and CPT Violation Effects in Muon Spin Precession. *Phys. Rev. Lett.* **2008**, *100*, 091602. [CrossRef]
11. Ulmer, S.; Smorra, C.; Mooser, A.; Franke, K.; Nagahama, H.; Schneider, G.; Higuchi, T.; Van Gorp, S.; Blaum, K.; Matsuda, Y.; et al. High-precision comparison of the antiproton-to-proton charge-to-mass ratio. *Nature* **2015**, *524*, 196–199. [CrossRef]
12. The ALICE Collaboration. Precision measurement of the mass difference between light nuclei and anti-nuclei. *Nat. Phys.* **2015**, *11*, 811–814. [CrossRef]
13. The ALICE Collaboration. Measurement of the Lifetime and Λ Separation Energy of ${}^{3}_{\Lambda}\mathrm{H}$. *Phys. Rev. Lett.* **2023**, *131*, 102302. [CrossRef]

14. The STAR Collaboration. Measurement of interaction between antiprotons. *Nature* **2015**, *527*, 345–348. [CrossRef]
15. The PAMELA Collaboration. The discovery of geomagnetically trapped cosmic ray antiprotons. *Astrophys. J. Lett.* **2011**, *737*, L29. [CrossRef]
16. The STAR Collaboration. Observation of the antimatter hypernucleus ${}^{4}_{\Lambda}\overline{\mathrm{H}}$. *Nature* **2024**, *632*, 1026–1031. [CrossRef]
17. Lattimer, J.M.; Prakash, M. The Physics of Neutron Stars. *Science* **2004**, 304, 409–412. [CrossRef]
18. Danysz, M.; Pniewski, J. Delayed disintegration of a heavy nuclear fragment: I. *Phil. Mag.* **1953**, 44, 348–350. [CrossRef]
19. The STAR Collaboration. Observation of an Antimatter Hypernucleus. *Science* **2010**, *328*, 58–62. [CrossRef]
20. The STAR Collaboration. Measurement of the mass difference and the binding energy of the hypertriton and antihypertriton. *Nat. Phys.* **2020**, 16 409–412. [CrossRef]
21. Chamberlain, O.; Segrè, E.; Wiegand, C.; Ypsilantis, T. Observation of Antiprotons. *Phys. Rev.* **1955**, *100*, 947–950. [CrossRef]
22. Cork, B.; Lambertson, G.R.; Piccioni, O.; Wenzel, W.A. Antineutrons Produced from Antiprotons in Charge-Exchange Collisions. *Phys. Rev.* **1956**, *104*, 1193–1197. [CrossRef]
23. Prowse, D.J.; Baldo-Ceolin, M. Anti-Lambda hyperon. *Phys. Rev. Lett.* **1958**, *1*, 179. [CrossRef]
24. Massam, T.; Muller, T.; Righini, B.; Schneegans, M.; Zichichi, A. Experimental observation of antideuteron production. *Nuovo Cim.* **1965**, *39*, 10–14. [CrossRef]
25. Dorfan, D.E.; Eades, J.; Lederman, L.M.; Lee, W.; Ting, C.C. Observation of Antideuterons. *Phys. Rev. Lett.* **1965**, *14*, 1003–1006. [CrossRef]
26. Vishnevsky, N.K.; Grachev, M.I.; Rykalin, V.I.; Lapshin, V.G.; Solyanik, V.I. Observation of antitritium. *Yad. Fiz* **1974**, *20*, 694–708.
27. Antipov, Y.M.; Denisov, S.P.; Donskov, S.V.; Gorin, Y.P.; Kachanov, V.A. Observation of antihelium-3. *Nucl. Phys. B* **1971**, *31*, 235–252. [CrossRef]
28. The STAR Collaboration. Observation of the antimatter helium-4 nucleus. *Nature* **2011**, *473*, 353–356. [CrossRef]
29. Chen, J.; Keane, D.; Ma, Y.G.; Tang, A.; Xu, Z. Anti nuclei in heavy ion collisions. *Phys. Repo.* **2018**, *760*, 1–39. [CrossRef]
30. Ackermann, K.H.; Adams, N.; Adler, C.; Ahammed, Z.; Ahmad, S.; Allgower, C.; Amonett, J.; Amsbaugh, J.; Anderson, B.D.; Anderson, M.; et al. STAR detector overview. *Nucl. Instrum. Methods A* **2003**, *499*, 624–632. [CrossRef]
31. The ALICE Collaboration. The ALICE experiment at the CERN LHC. *J. Instrum.* **2008**, *3*, S08002. [CrossRef]
32. The ALICE Collaboration. First Measurement of $A = 4$ Hypernuclei and Antihypernuclei at the LHC. *Phys. Rev. Lett.* **2025**, *134*, 162301. [CrossRef]
33. Hans, B. A method to improve tracking and particle identification in TPCs and silicon detectors. *Nucl. Instrum. Methods A* **2006**, *562*, 154–197. [CrossRef]
34. The STAR Collaboration. Measurements of Proton High-Order Cumulants in $\sqrt{s_{NN}} = 3$ GeV Au+Au Collisions and Implications for the QCD Critical Point. *Phys. Rev. Lett.* **2022**, *128*, 202303. [CrossRef]
35. The STAR Collaboration. Precision Measurement of (Net-)proton Number Fluctuations in Au+Au Collisions at RHIC. *Phys. Rev. Lett.* **2025**, *135*, 142301. [CrossRef]
36. The STAR Collaboration. Beam Energy Dependence of Triton Production and Yield Ratio ($N_t \times N_p / N_d^2$) in Au + Au Collisions at RHIC. *Phys. Rev. Lett.* **2023**, *130*, 202301. [CrossRef]
37. The STAR Collaboration, Onset of Constituent Quark Number Scaling in Heavy-Ion Collisions at RHIC. *Phys. Rev. Lett.* **2025**, *135*, 072301. [CrossRef]
38. The STAR Collaboration. Global Λ hyperon polarization in nuclear collisions. *Nature* **2017**, *548*, 62–65. [CrossRef]
39. The STAR Collaboration. Pattern of global spin alignment of ϕ and K_0^* mesons in heavy-ion collisions. *Nature* **2023**, *614*, 244–248. [CrossRef]
40. The ALICE Collaboration. Alignment of the ALICE Inner Tracking System with cosmic-ray tracks. *J. Instrum.* **2010**, *5*, P03003. [CrossRef]
41. The ALICE Collaboration. The ALICE TPC, a large 3-dimensional tracking device with fast readout for ultra-high multiplicity events. *Nucl. Instrum. Methods A* **2010**, *622*, 316–367. [CrossRef]
42. The ALICE Collaboration. Observation of deuteron and antideuteron formation from resonance-decay nucleons. *Nature* **2025**, *648*, 306–311. [CrossRef]
43. The ALICE Collaboration. Evidence of Spin-Orbital Angular Momentum Interactions in Relativistic Heavy-Ion Collisions. *Phys. Rev. Lett.* **2020**, *125*, 012301. [CrossRef]
44. The ALICE Collaboration. First measurement of D*+ vector meson spin alignment in Pb–Pb collisions at $\sqrt{s_{NN}}$ = 5.02 TeV. *J. High Energ. Phys.* **2025**, *2025*, 94. [CrossRef]
45. The ALICE Collaboration. Investigations of Anisotropic Flow Using Multiparticle Azimuthal Correlations in pp, $p-$Pb, Xe-Xe, and Pb-Pb Collisions at the LHC. *Phys. Rev. Lett.* **2019**, *14*, 142301. [CrossRef]
46. The ALICE Collaboration. Unveiling the strong interaction among hadrons at the LHC. *Nature* **2020**, *588*, 232–238. [CrossRef]
47. The ALICE Collaboration. Study of $(\langle p_{\mathrm{T}} \rangle)$ and its higher moments, and extraction of the speed of sound in Pb-Pb collisions with ALICE. *J. High Energ. Phys.* **2025**, *2025*, 76. [CrossRef]

48. Cowan, G.; Cranmer, K.; Gross, E.; Vitells, O. Asymptotic formulae for likelihood-based tests of new physics. *Eur. Phys. J. C* **2011**, *871*, 1544. [CrossRef]
49. Abdallah, M.S.; Aboona, B.E.; Adam, J.; Adamczyk, L.; Adams, J.R.; Adkins, J.K.; Agakishiev, G.; Aggarwal, I.; Aggarwal, M.M.; Ahammed, Z.; et al. Measurements of $^{3}_{\Lambda}$H and $^{4}_{\Lambda}$H Lifetimes and Yields in Au + Au Collisions in the High Baryon Density Region. *Phys. Rev. Lett.* **2023**, *128*, 202301. [CrossRef]
50. Sato, H.; Yazaki, K. On the coalescence model for high energy nuclear reactions. *Phys. Lett. B* **1981**, *98*, 153–157. [CrossRef]
51. Andronic, A.; Munzinger, P.B.; Stachel, J.; Stöcker, H. Production of light nuclei, hypernuclei and their antiparticles in relativistic nuclear collisions. *Phys. Lett. B* **2011**, *697*, 203–207. [CrossRef]
52. The ALICE Collaboration. Production of ^{4}He and $^{4}\overline{\text{He}}$ in Pb–Pb collisions at $\sqrt{s_{NN}}$= 2.76 TeV at the LHC. *Nucl. Phys. A* **2018**, *971*, 1–20. [CrossRef]
53. Vovchenko, V.; Dönigus, B.; Stoecker, H. Multiplicity dependence of light nuclei production at LHC energies in the canonical statistical model. *Phys. Lett. B* **2018**, *785*, 171–174. [CrossRef]
54. Steinheimer, J.; Gudima, K.; Botvina, A. Hypernuclei, dibaryon and antinuclei production in high energy heavy ion collisions: Thermal production vs. Coalescence. *Phys. Lett. B* **2012**, *714*, 85–91. [CrossRef]
55. The STAR Collaboration. Identified Baryon and Meson Distributions at Large Transverse Momenta from Au+Au Collisions at $\sqrt{s_{NN}}$ = 200 GeV. *Phys. Rev. Lett.* **2006**, *97*, 152301. [CrossRef]
56. The ALICE Collaboration. $^{3}_{\Lambda}$H and $^{3}_{\Lambda}\overline{\text{H}}$ production in Pb–Pb collisions at $\sqrt{s_{NN}}$ = 2.76 TeV. *Phys. Lett. B* **2016**, *754*, 360. [CrossRef]
57. The ALICE Collaboration. Measurement of (anti)alpha production in central Pb–Pb collisions at $\sqrt{s_{NN}}$ = 5.02 TeV. *Phys. Lett. B* **2024**, *858*, 138943. [CrossRef]
58. Pérez-Obiol, A.; Gazda, D.; Friedman, E.; Gal, A. Revisiting the hypertriton lifetime puzzle. *Phys. Lett. B* **2020**, *811*, 135916. [CrossRef]
59. Rayet, M.; Dalitz, R.H. The lifetime of $^{3}_{\Lambda}$H. *Nuovo. Cim. A* **1966**, *46*, 786. [CrossRef]
60. Gongleton, J.G. A simple model of the hypertriton. *J. Phys. G: Nucl. Part. Phys.* **1992**, *18*, 339. [CrossRef]
61. Kamada, H.; Golak, J.; Miyagawa, K.; Witała, H.; Glöckle, W. π-mesonic decay of the hypertriton. *Phys. Rev. C* **1998**, *57*, 1595. [CrossRef]
62. Gal, A.; Garcilazo, H. Towards resolving the $^{3}_{\Lambda}$H lifetime puzzle. *Phys. Lett. B* **2019**, *791*, 48. [CrossRef]
63. Prem, R.J.; Steinberg, P.H. Lifetimes of Hypernuclei, $^{3}_{\Lambda}$H, $^{4}_{\Lambda}$H, $^{5}_{\Lambda}$H. *Phys. Rev.* **1964**, *136*, B1803. [CrossRef]
64. Keyes, G.; Derrick, M.; Fields, T.; Hyman, L.G.; Fetkovich, J.G.; McKenzie, J.; Riley, B.; Wang, I.-T. New Measurement of the $^{3}_{\Lambda}$H Lifetime. *Phys. Rev. Lett.* **1968**, *20*, 819. [CrossRef]
65. Phillips, R.E.; Schneps, J. Lifetimes of Light Hyperfragments. II. *Phys. Rev.* **1969**, *180*, 1307. [CrossRef]
66. Keyes, G.; Derrick, M.; Fields, T.; Hyman, L.G.; Fetkovich, J.G.; McKenzie, J.; Riley, B.; Wang, I.-T. Properties of $^{3}_{\Lambda}$H. *Phys. Rev. D* **1970**, *1*, 66. [CrossRef]
67. Keyes, G.; Sacton, J.; Wickens, J.H.; Block, M.M. A measurement of the lifetime of the $^{3}_{\Lambda}$H hypernucleus. *Nucl. Phys. B* **1973**, *67*, 269. [CrossRef]
68. Avramenko, S.; Aksinenko, V.; Anikina, M.; Bannik, B.; Belikov, Yu.; Butenko, V.; Drozdov, V.; Gajevski, K.; Galperin, A.; Glagoleva, N.; et al. A study of the production and lifetime of the lightest relativistic hypernuclei. *Nucl. Phys. A* **1992**, *547*, 95. [CrossRef]
69. Rappold, C.; Kim, E.; Nakajima, D.; Saito, T.R.; Bertini, O.; Bianchin, S.; Bozkurt, V.; Kavatsyuk, M.; Ma, Y.; Maas, F.; et al. Hypernuclear spectroscopy of products from ^{6}Li projectiles on a carbon target at 2 AGeV. *Nucl. Phys. A* **2013**, *913*, 170. [CrossRef]
70. Bohm, G.; Klabuhn, J.; Krecker, U.; Wysotzki, F.; Coremans, G.; Sacton, J.; Vilain, P.; Wickens, J.H.; Wilquet, G.; O'Sullivan, D.; et al. On the lifetime of the $^{3}_{\Lambda}$H hypernucleus. *Nucl. Phys. B* **1970**, *16*, 46. [CrossRef]
71. The STAR Collaboration. Measurement of the $^{3}_{\Lambda}$H lifetime in Au+Au collisions at the BNL Relativistic Heavy Ion Collider. *Phys. Rev. C* **2018**, *97*, 054909. [CrossRef]
72. ALICE Collaboration. $^{3}_{\Lambda}$H and $^{3}_{\Lambda}\overline{\text{H}}$ lifetime measurement in Pb-Pb collisions at $\sqrt{s_{NN}}$ = 5.02 TeV via two-body decay. *Phys. Lett. B* **2019**, *797*, 134905. [CrossRef]
73. Gal, A. Recent progress on few-body hypernuclei. *EPJ Web of Conf.* **2022**, *259*, 08002. [CrossRef]
74. Outa, H.; Aoki, M.; Hayano, R.S.; Ishikawa, T.; Iwasaki, M.; Sakaguchi, A.; Takada, E.; Tamura, H.; Yamazaki, T. Mesonic weak decay of $^{4}_{\Lambda}$H and $^{4}_{\Lambda}$He. *Nucl. Phys. A* **1995**, *585*, 109. [CrossRef]